Failure and strain gradient analyses in incremental forming using GTN model

Muhammad Ilyas, Ghulam Hussain, Christine Espinosa

Failure and strain gradient analyses in incremental forming using GTN model

Muhammad Ilyas [a, *], Ghulam Hussain [a], Christine Espinosa [b]

[a] Faculty of Mechanical Engineering, GIK Institute of Engineering Sciences and Technology, Topi, 23460, Pakistan
[b] 2033, Espace Clement Ader, 3 rue Caroline Aigle, 31400, Toulouse, France

ARTICLE INFO

Keywords:
Single point incremental forming
SPIF
GTN damage model
Failure prediction
Formability

ABSTRACT

Single point incremental forming (SPIF) process is gaining popularity for rapid manufacturing of complex 3D shapes. The present study is aimed at numerically predicting the failure using the Gurson-Tvergaard-Needleman (GTN) model and further clarifying the deformation mechanics in SPIF. Deformation mechanics and failure in SPIF process are examined numerically by simulating a straight groove test. Solid finite element (FE) models have been employed to investigate deformation modes. The GTN damage model has successfully predicted forming limits in the straight groove test. It is shown that failure, regardless of the incremental sheet forming (ISF) conditions, occurs when the damage parameter (d) approaches one. Furthermore, effective plastic strain, hydrostatic pressure, vertical tool force and through thickness strain gradient increase with an increase in step size. Finally, it is shown that an increase in hydrostatic pressure and increase in through thickness strain gradient enhance formability.

1. Introduction

Single point incremental forming (SPIF) is gaining popularity for rapid manufacturing of highly customized parts to be produced in small lots for various transportation and biomedical applications. SPIF is flexible and economical, compared to conventional stamping, as sheet deformation is carried out by a cylindrical rod with a spherical end, thus eliminating the requirement of dedicated dies. The flexibility and simplicity have engendered an ever-increasing focus on research over the years. The majority of research has focused on understanding applications [1,2], geometric accuracy [3], deformation mechanisms [4,5], formability [6] and process parameters [7].

SPIF method was patented by Leszak [8] in 1967. Academic research on the process was initiated in Japan in the 90s, [9,10]. Zheng et al. [11] reviewed various forming techniques for lightweight aluminum alloys. They concluded that single point incremental forming enables the manufacturers to produce complex shapes. The major focus of research on incremental forming has been on identifying mechanics underlying enhanced formability and evolution of plastic deformation. Effect of tool type, size, feed rate and friction on formability was investigated by experiments and, simultaneously, finite element analyses were performed by Kim and Park, [12]. They recommended that the straight groove test can be used to assess the formability. Experimental investigation of SPIF mechanics was conducted by Jackson and Allwood, [13]. The authors concluded that fundamental deformation mechanisms are bending, stretching and shear. Furthermore, it was shown that shear parallel and perpendicular, to tool motion, are higher in incremental forming than other conventional forming processes. Jackson and Allwood [13] proposed that increased formability may be caused by increasing shear during plastic deformation. Emmens and van den Boogaard [14] discussed six mechanisms to understand deformation mechanics and influence on increased formability in ISF. They concluded that contact stresses, simultaneous bending, and tension combined with the shear play crucial role in immense localized deformation. Furthermore, cyclic straining and hydrostatic stress influence the delayed necking. McAnulty et al. [6] conducted a quantitative literature review and analyzed experimental results from literature which focused upon the influence of SPIF process parameters on formability. They summarized that parameters vis-à-vis material thickness, tool size, spindle speed, and feed rate should be optimized, taking the mutual interaction of these parameters into account. Al-Ghamdi and Hussain [15] conducted a study to characterize operating conditions that maximize

* Corresponding author.
E-mail addresses: ilyas@giki.edu.pk (M. Ilyas), ghulam.hussain@giki.edu.pk (G. Hussain), christine.espinosa@isae-supaero.fr (C. Espinosa).

formability in SPIF and lead to stable plastic deformation without any undue surface cutting. They concluded that tool radius and blank thickness are closely related to ensure stable deformation. Most of the previous works focused on historical development and deformation mechanisms of SPIF, while failure prediction needs special attention. Therefore, it is a useful addition to have a dedicated study on the prediction of failure in the SPIF process and carry the process to successive technological maturity.

In sheet forming, the failure occurs due to a combination of mechanisms including, void nucleation and coalescence, shear band formation and plastic instability, [16]. In order to understand the development of failure in SPIF, deformation modes and states of stress and strain in the localized deformation zone should be known. SPIF manifests more than one deformation modes such as plane strain stretching situation in flat surfaces, plane strain stretching occurring in rotational symmetric surfaces and equal bi-axial stretching taking place at corners [5]. Martins et al. [17] have presented a closed-form analysis modeling the fundamentals of SPIF. Their model takes into account ductile damage but is limited as it is based on membrane analysis. Experiments performed by Martins et al. [17] combined with findings recovered from literature confirmed that their proposed theoretical work was adept to address the effect of major forming parameters and explain enhanced formability of SPIF. Another analytical model developed, for SPIF, by Fang et al. [18] is capable of describing the localized mechanics of deformation and fracture behavior. Their model takes into account the bending effect and strain hardening. But it is based on plane strain assumptions, therefore, inherently lacks to take into account the 3-D state of strain.

Lin et al. [19] have presented a review of the development of micro-damage under various deformation conditions. Zhang et al. [20] have presented a review on modeling techniques for prediction of forming limit diagrams (FLDs). They concluded that continuum damage mechanics based models are capable of predicting sheet metal FLDs. Wu et al. [21] have applied an isotropic Lemaitre model for damage prediction in incremental forming. The Gurson-Tvergaard-Needleman (GTN) approach is based on void mechanics and is one of the well-known models for ductile fracture, [20,22]. Gologanu et al. [23] extended the GTN model, which was later successfully applied by Brunet et al. [24] to determine classical forming limit diagrams (FLDs) of Ni-based sheet metal and an aluminum alloy. Hirt et al. [25] have applied the GTN model to qualitatively determine the damage in incremental forming. Very recently, some efforts have been dedicated to the application of GTN model in incremental forming, [26–28].

From the previous discussion, it is concluded that enhanced formability, in particular, the influence of strain gradient upon enhanced formability needs to be further explored. Therefore, in the present paper, the GTN model is applied to predict failure in incremental forming and enhance understanding of deformation mechanics under various conditions. Fracture is predicted in straight groove test. Solid finite element (FE) models have been employed. Step size and sheet thickness are varied and deformation characteristics namely, effective plastic strain, hydrostatic pressure, damage, tool forces, minimum principal strain gradient, shear strains, and forming limits are quantified. The relationship between through thickness strain gradient and enhancement of formability is a salient finding of this study.

2. Experimental setup

In the present study a 1.5 *mm* thick AA-2024O sheet, was employed. The specimens were cut from this sheet in the rectangular shape of 120 *mm* × 60 *mm*. The sheet was clamped in a fixture, as shown in Fig. 1, and forming area was 100 *mm* × 40 *mm*. A hemispherical head tool with radius 8 *mm*, made of tool steel, traveled back and forth a distance of 60 *mm* under a constant feed rate of 10 *mm* per second with fixed step size normal to the plane of the sheet. The sheet was then removed from the fixture and major and minor strains were measured from the grids (1.5 *mm* × 1.5 *mm*) which had been printed on the non-contact side.

3. Finite Element Modeling

3.1. Constitutive law and model validation

Dog bone specimen of AA-2024O blank, according to ASTM-E8 [29], were prepared and tested in a universal testing machine. Results of a typical test are shown in Fig. 2. The physical parameters, elastic modulus and, yield stress were determined from these tests and are summarized in Table 1.

The force-displacement curve, obtained from experiment, was then converted to true stress-strain curve and the results are shown in Fig. 3. The experiment was simulated by the commercial FEA software, LS-Dyna®, and this curve was input via the piecewise linear elastic-plastic material model available in the software. The results obtained from the simulation of a uniaxial test were compared with experimental test results. A good comparison was obtained as depicted in Fig. 2.

Gurson flow function is defined as:

$$\phi = \frac{\sigma_M^2}{\sigma_Y^2} + 2q_1 f^* \cosh\left(\frac{3q_2\sigma_H}{2\sigma_Y}\right) - 1 - \left(q_1 f^*\right)^2 = 0$$

Here, σ_M is the equivalent von Mises Stress, σ_Y is yield stress, σ_H is the mean hydrostatic stress and is defined as $(\sigma_1+\sigma_2+\sigma_3)/3$. σ_1, σ_2, and σ_3 are principal stresses. The effective void volume fraction is defined as:

$$f^*(f) = \begin{cases} f & f \le f_c \\ f_c + \dfrac{1/q_1 - f_c}{f_F - f_c}(f - f_c) & f > f_c \end{cases}$$

The quantities denoted as q_1, q_2, f_c, and f_F are constitutive material constants as described in Refs. [31,32]. For the parameter f, its time derivative ($\dot{f}$) sums the growth of existing voids $\dot{f}_G$ and void nucleation rate $\dot{f}_N$i.e.

$$\dot{f} = \dot{f}_G + \dot{f}_N$$

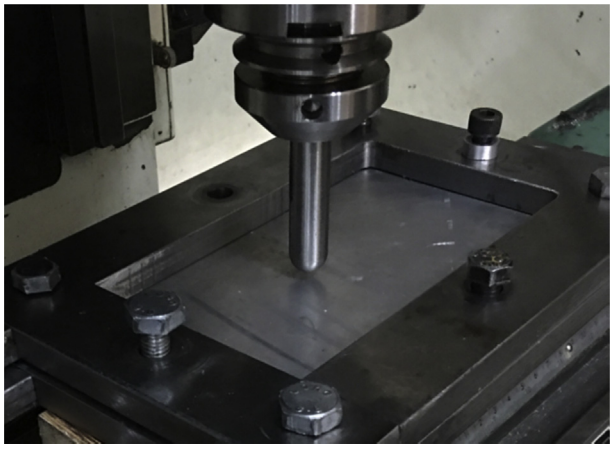

Fig. 1. A straight groove test specimen clamped below the hemispherical head tool.

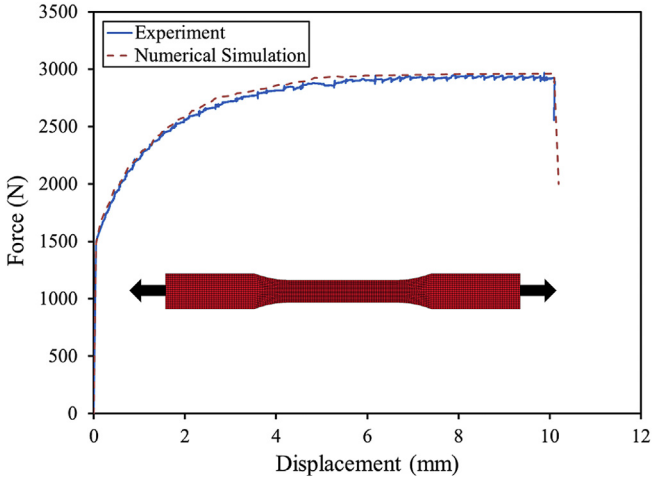

Fig. 2. Uniaxial test, comparison of experimental and numerical force vs. displacement curves.

Table 1
Material properties of AA−2024O for FEA, [30].

Density,ρ (kg/mm^3)	Young's Modulus,E (GPa)	Poisson's ratio, ν	Yield stress,σ_y (MPa)
2730	73	0.3	80

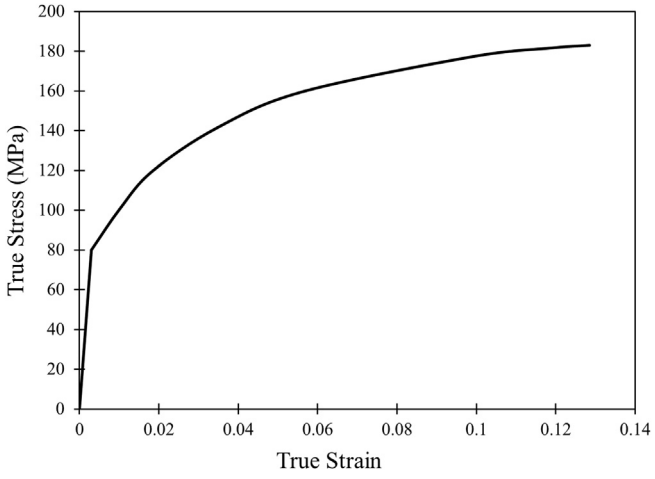

Fig. 3. True Stress-Strain curve for AA−2024O material used in FEA.

The growth of existing voids is a function of principal strain rates:

$$\dot{f}_G = (1-f)\dot{\varepsilon}^p_{kk}$$

And void nucleation rate $\dot{f}_N = A\dot{\varepsilon}_p$, where function A is defined as.

Table 2
GTN material properties, [33].

q_1	q_2	f_c	f_0	ε_N	S_N	f_N	f_F
1.5	1.0	0.0035	0.002	0.4	0.1	0.01	0.16

$$A = \frac{f_N}{S_N\sqrt{2\pi}}\exp\left(-\frac{1}{2}\left(\frac{\varepsilon_p-\varepsilon_N}{S_N}\right)^2\right)$$

Here f_N, S_N, and ε_N are material constants and voids are nucleated only in tension. The dimensionless material damage parameter d is expressed as:

$$d = \frac{f-f_0}{f_F-f_0}$$

GTN material parameters used in the present study are shown in Table 2. The same parameters were used for the simulation of uniaxial test presented earlier and line test which will be presented in the coming paragraphs.

3.2. Finite Element Model of line test

Numerical simulations by finite element method were performed using commercial finite element code LS-Dyna®. LS-Dyna® was selected for finite element analysis due to its well-recognized status in solving problems involving contact and large deformations at better computational speed, [34].

3.2.1. Spatial discretization and tool path

The SPIF process manifests, notably, immense shear deformations. Therefore, solid elements are employed for the meshing of the sheet. Eight-node, hexahedron, solid elements with one integration point are used to speed up the calculation and circumvent the problem of shear locking observed in fully integrated elements. Thickness direction is discretized by three elements. In the present study, 100 elements along length and 40 along the width, respectively, are used to represent the blank which results in a total of 12,000 solid elements. Stiffness-based hourglass control formulation for explicit finite elements is turned on to diminish the effect of zero-energy deformation modes that may develop during numerical simulation of sheet deformation and render the numerical results unusable. Furthermore, two sheet thicknesses, 0.75 *mm* and 1.0 *mm*, were considered and are represented by the symbol "ts".

In the current study, the outer periphery of the model was constrained by restricting all the three degrees of freedom of nodes in *x*, *y* and *z* directions to impede the material from flowing during the forming process. This is identical to the clamping of blank boundaries realized during actual tests. The complete meshed model employed in this study is presented in Fig. 4 (a).

Hemispherical head forming tool, with radius 8 *mm*, was meshed by the rigid shell (quad) elements. To ensure better representation of curved tool surface, repartition of nodal forces and contact conditions, the forming tool element size was slightly less than 1 *mm* × 1 *mm*. The relative sliding behavior at the contact interfaces between forming tool and blank was modeled by Coulomb's law of friction. Oil lubricant was used during actual tests and a frictional coefficient of $f_s = 0.18$ was used in the numerical calculations to represent steel/aluminum contact, [4]. Furthermore, segment-based contact with warped segment checking in sliding option was activated. The forming tool was constrained to move only in *xz*-plane. A schematic of the tool-path is presented in Fig. 4 (b). It is worth noting that (two different) step down sizes 0.5 mm and 1.0 mm are studied. Step down is represented by the symbol "Pz".

3.2.2. Simulation time

Stability of the explicit integration algorithm is limited by the time step size [35]. Traditionally, this type of algorithm is more

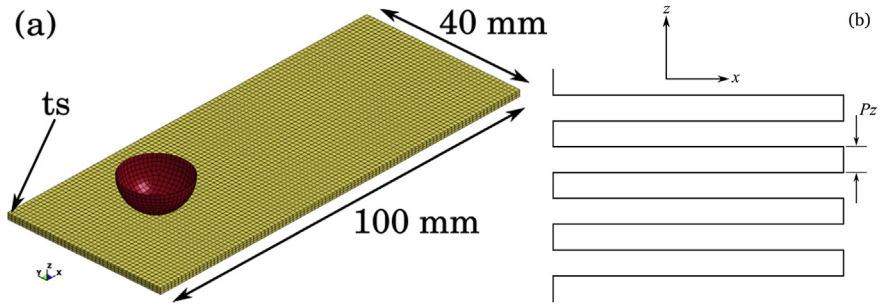

Fig. 4. Finite Element Model of single groove test (a) meshed plate and tool (b) tool path.

suitable for rapid dynamic simulations. However, it can be applied to simulate nonlinear, large deformation and contact of multiple deformable bodies. All these factors combine to the selection of the explicit method for numerical simulation.

It is important to find an appropriate time duration for the virtual experiment that engenders numerical results comparable to experimental ones. Nevertheless, this modification must not generate numerical artifacts such as kinetic energy due to spurious oscillations which pollute the numerical results.

For the strain rates under consideration, the material behavior is independent of strain rate, [36]. Therefore, the simulation time was chosen to be of appropriate length. Several simulations were carried out with higher tool feed to identify the smallest time which does not introduce spurious numerical effects. Finally, a simulation time of 0.06 *sec* was chosen, which lead to a tool feed rate of 10 m/sec. Similarly, the tool travel in the z-direction, step down speed, was 10 m/sec.

3.2.3. *Fracture in the line test*

The value of damage parameter d, as defined in the GTN model, varies from 0 to 1. These values represent fully intact and fractured material states, respectively. Fig. 5 shows a contour plot of damage variable d for a typical 100 $mm \times 40$ mm blank from the top. We observe that fracture occurs below the tool as shown by a red circle. As soon as the value of damage parameter d reaches 1 in an element, it is deleted from the calculation by applying element kill technique to represent the fracture.

4. Results and discussion

In order to investigate the local deformation behavior in straight groove test, elements on the inner surface (in contact with tool) and the outer surface (not in contact with tool) were selected, see Fig. 6 for this definition and location. It was observed that fracture always occurred at corner, this location has been highlighted in the same figure. The element numbers for one typical simulation

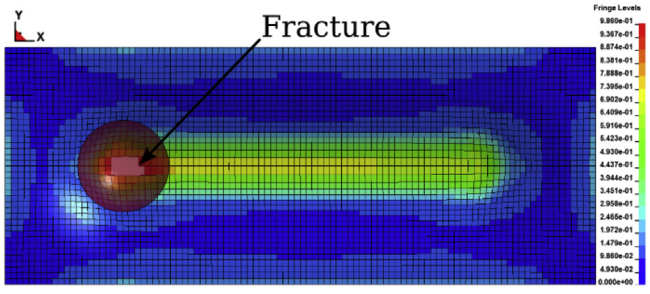

Fig. 5. Contour plot of damage variable, d, showing fracture predicted by FEA.

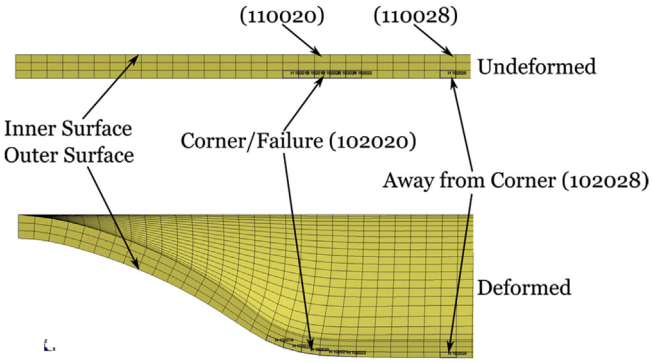

Fig. 6. Section view showing element locations in an undeformed and deformed blank.

representing the locations are also shown in the figure. Results at the corner and away from the corner will be analyzed in the following paragraphs.

To understand the deformation mechanics and damage evolution in SPIF, some key deformation indicators were analyzed. These indicators include effective plastic strain (ε_p), hydrostatic pressure (p), shear strain parallel to tool travel direction (ε_{23}), shear strain perpendicular to tool travel direction (ε_{13}) and damage variable (d). These indicators are plotted for inner and outer elements as shown in following the figures.

4.1. *Effective plastic strain*

Evolution of effective plastic strain, ε_p, as a function of forming depth is plotted in Fig. 7. The figure illustrates the inherent mechanics of incremental forming that effective plastic strain is

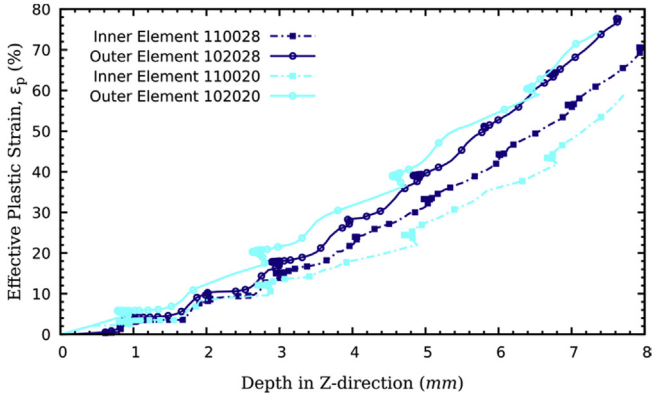

Fig. 7. Plastic strain (ε_p) in elements at and away from the corner, as a function of forming depth (ts = 1.5 mm).

increasing with forming depth for all the elements under consideration. The plastic strain development gradually evolves with each incremental pass. The elements located at the inner surface of the blank exhibit lower value of plastic strain, while those located on the outer surface show higher plastic strain. This difference indicates the existence of the local bending effect, as shown by Ref. [13]. This can be explained by the bending theory, [37], the inner surface elements are being compressed while outer surface elements are being stretched.

A comparison of plastic strain accumulation in elements across the thickness for different step sizes (represented by the symbol Pz) and sheet thickness (ts) is shown in Fig. 8. For same sheet thickness, it can be seen that the plastic strain prior to fracture increases from 59% to 67% in the inner element at the corner, Fig. 8(a), with a decrease in step size from 1.0 *mm* to 0.5 *mm*. It is further observed that the magnitude of increase in plastic strain is more for the inner element as compared with the increase for the middle or outer element. Moreover, the decrease in sheet thickness from 1.0 *mm* to 0.5 *mm*, manifests itself as a decrease in plastic strain accumulation, which is contrary to the decrease in step size.

Away from the corner, Fig. 8(b), plastic strain decreases for both: the decrease in step size as well as sheet thickness. The decrease is more than 10% for elements on the inner and outer surface. This can be attributed to biaxial stretching at corner as compared with the plane strain compression away from the corner.

4.2. Hydrostatic pressure

Fig. 9 shows hydrostatic pressure evolution as a function of time. Overall, the tension-compression behavior of bending case manifests a negative value of hydrostatic pressure in the inner surface and positive value in the outer surface. The isolated peaks at start and end of loop enclose stable regions during horizontal tool travel. The peaks can be neglected as these occur during the step down when the tool pushes vertically down into the plane of the blank. During the start i.e. between $1-10$ *msec*, compression and tension observed are approximately equal. The difference between these two values decreases with the passage of time. As the tool performs a straight groove in the blank, the elements lying perpendicular to the tool motion start sharing the contact force and the hydrostatic pressure is distributed in the contact elements, see Fig. 9(a) between $38-48$ *msec*. This decrease is more pronounced in the inner surface elements as compared with the outer surface elements.

A summary of hydrostatic pressure developed, in elements at corner and away from the corner, at the start of the simulation and before the fracture is presented in Table 3. Hydrostatic pressure is more at the corner than away from the corner. Furthermore, the magnitude of hydrostatic pressure, although compressive in nature, is higher in inner elements as compared with outer elements which are in tension, for the thicker sheet. Whereas, for thinner sheet, the magnitude of hydrostatic pressure exhibits little variation for inner and outer elements. Additionally, the magnitude of hydrostatic pressure, in inner elements, decreases with the passage of time for all the set of parameters considered in the present study. While, in outer elements of the thicker sheet (ts $= 1.0$ *mm*), the hydrostatic pressure decreases and for the thinner sheet (ts $= 0.75$ *mm*), the hydrostatic pressure increases, irrespective of step size. This behavior can be attributed to relatively higher stretching experienced by the thinner sheet.

4.3. Damage

Fig. 10 shows the evolution of damage variable, d, with respect to time. For the inner and outer surface elements the damage variable increases in steps. The gap between the two elements is small at the start and increases with the passage of time for corner element. The same is not true for an element located away from the corner.

It is further noticed that the fracture occurs at the corner during the step-down, when the tool pushes vertically down, the damage variable, d, shoots to the value of 1. Away from the corner, the value of damage variable is ≈ 0.8 for inner element and ≈ 0.85 for the outer element. The fracture predicted by FEA starts from the outer surface and then propagates toward inner surface, this is in agreement with the experimental observations.

Damage accumulation in elements across the thickness for different step sizes and thickness is shown in Fig. 11. The decrease in step size from 1 *mm* to 0.5 *mm* results in a lower value of damage at both locations (i.e. corner and away from the corner). While the change in thickness from 1.5 *mm* to 0.75 *mm* does not cause the damage parameter to vary significantly.

4.4. Tool force

The evolution of the tool force reported is plotted in Fig. 12. For all the cases studied here, it is observed that the tool forces keep on increasing and stabilize before fracture. The decrease in step-size results in a lower magnitude of forces exerted by the tool which is similar to the observation for the case of the thinner sheet. This difference can be attributed to the decrease in stiffness of the tool-blank system with a decrease in step-size and sheet thickness. These results are in agreement with a previous experimental study conducted by Al-Ghamdi and Hussain [38].

4.5. Minimum principal strain gradient

Fig. 13 shows the evolution of the gradient of the minimum principal strain. This value was obtained by subtracting the

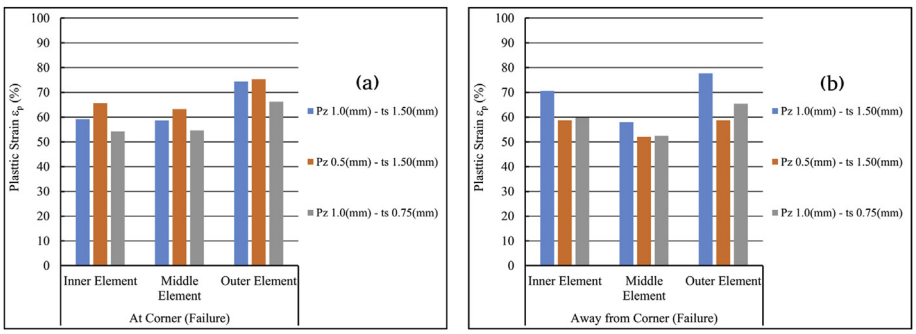

Fig. 8. Comparison of plastic strain before fracture, (a) at corner/failure and (b) away from the corner/failure.

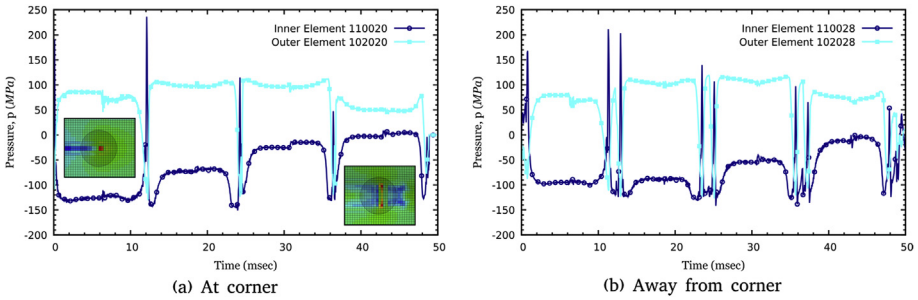

Fig. 9. Comparison of plastic strain (a) at corner and (b) away from the corner before fracture takes place (ts = 1.5 mm).

Table 3
Summary of hydrostatic pressure (p in MPa) in elements under consideration.

Forming parameters		At corner		Away from the corner	
	Element location	Start of simulation	Before fracture	Start of simulation	Before fracture
Pz 1.0 mm	Inner element	−130	5	−95	−10
ts 1.5 mm	Outer element	85	50	80	70
Pz 0.5 mm	Inner element	−120	−5	−90	−5
ts 1.5 mm	Outer element	75	45	70	65
Pz 1.0 mm	Inner element	−75	60	−70	−5
ts 0.75 mm	Outer element	75	80	70	80

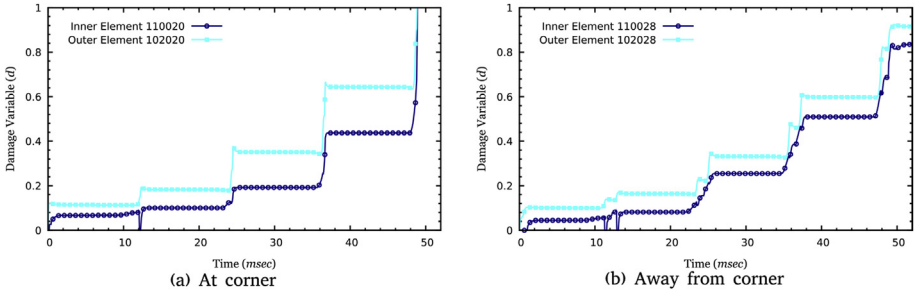

Fig. 10. Damage variable, d, as a function of time (ts = 1.5 mm).

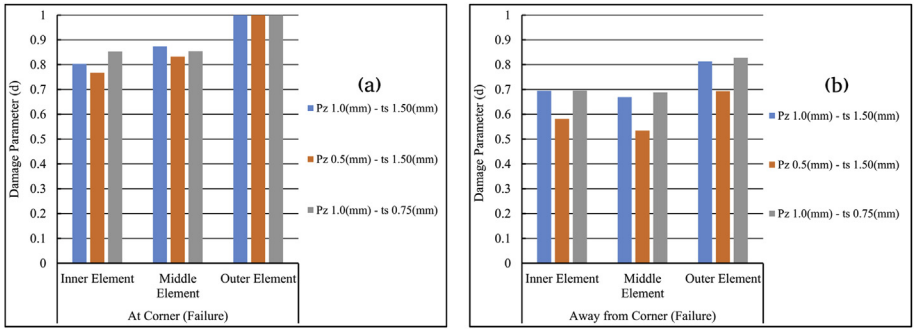

Fig. 11. Comparison of damage at and away from corner/failure.

minimum principal strain of outer element from the minimum principal strain of inner element. These graphs are plotted until the last value obtained before the fracture is predicted by the software. The strain gradient depicts stable zones between fluctuations occurring due to step-down. These stable zones ascend in steps, reach a peak stable value and then descend prior to fracture. For different values of step-down and sheet thickness, it is observed that the peak value of this gradient is more for an element at corner as compared with the element away from the corner. In the stable zone, prior to fracture, for a step-size of 1 *mm* and sheet thickness 1.5 *mm*, the strain gradient at corner is 0.072 (7.2%) and away from the corner is 4.8%. While, for the step-size of 0.5 *mm* and same sheet thickness, the strain gradient remains identical i.e. 4.5 %. Moreover, for the step-size of 1 *mm* and sheet thickness of 0.75 *mm*, the strain gradient at corner is 4.2 % and away from the corner is 2.4 %. The descent in the strain gradient can be attributed

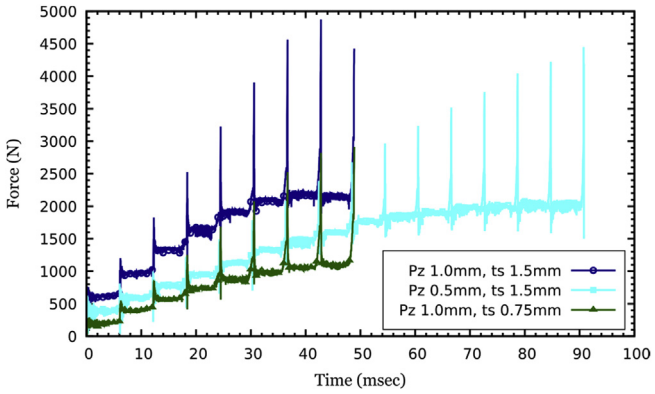

Fig. 12. Comparison of tool forces.

to the fact that the contact area has increased towards the fracture as compared with the start of the simulation.

4.6. Shear strain parallel to tool travel direction

The evolution of shear strain (ε_{23}) parallel to the horizontal direction of tool motion is plotted in Fig. 14. The magnitude of shear in elements near the corner, see Fig. 14(a), is higher as compared with the shear strain in elements away from the corner, see Fig. 14(b). The peaks in both locations occur at a similar instance of time, this can be attributed to the step down i.e. when the tool pushes vertically into the plane of the blank. Another trend is visible in Fig. 14(b) i.e. the higher shearing experienced by the inner element during the start of simulation as compared with the outer element. As the simulation progresses, the tool becomes immersed in the sheet, shear in outer elements becomes more than the inner element at the corner. This difference can be attributed to biaxial stretching in the corner region as already reported by Silva et al. [39].

4.7. Shear strain perpendicular to tool travel direction

The shear strain (ε_{13}) perpendicular to horizontal tool motion is plotted in Fig. 15. Inner elements, both at the corner and away from the corner, experience higher shear as compared with outer elements. Furthermore, shear perpendicular to tool travel is higher than that parallel to it. This observation is different as compared with results already reported by Li et al. [4] and Smith et al. [40]. The difference can be attributed to the mixed stress-strain state due to blank geometry of straight groove test. In contrast with the shear parallel to tool motion, shear perpendicular to tool motion is nearly identical, at and away from the corner, before fracture.

4.8. Forming limit prediction

The forming limit diagram (FLD), developed by Keeler and Backhofen, [41], has been widely used for failure diagnosis in sheet metal forming. This diagram is essentially dependent upon the strain state and not on the boundary conditions. The FLD is obtained by plotting a graph of the major strain (ε_{11}) vs. minor strain (ε_{22}). The detailed procedure of its construction can be found in Marciniak et al. [37]. Forming limits predicted by the GTN model are shown in Fig. 16. The GTN model used in the present study, predicts 7% lower values of forming limit as compared with the experiment, see Fig. 16(a). A comparison of experimental and numerical results for different combinations of step sizes and sheet thickness is shown in Fig. 16(b). It is further observed that the formability decreased with a decrease in step size, from 1 *mm* to 0.5 *mm*. Similarly, for the case of a thinner sheet, the decrease in formability is 1%, which is not significant.

The forming limits predicted by GTN model are in close agreement with the experimental values for the set of parameters studied. The difference between experimental and numerical

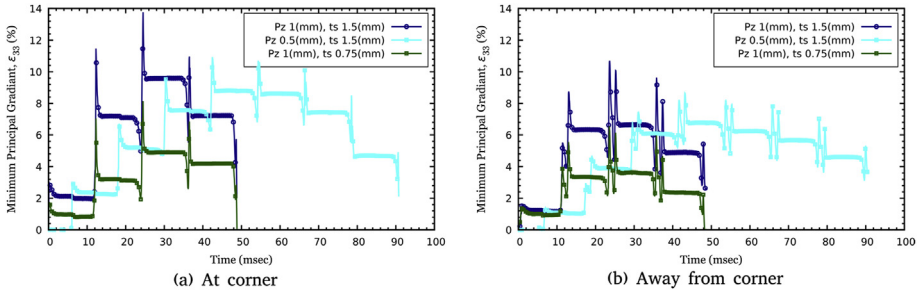

Fig. 13. Gradient of (through thickness) minimum principal strain (ε_{33}).

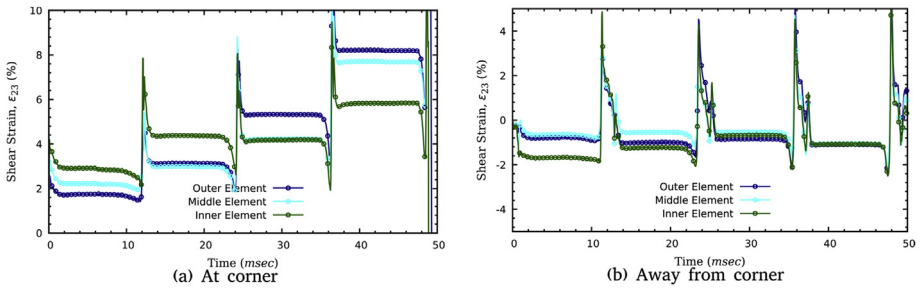

Fig. 14. Shear strain (ε_{23}) parallel to tool motion.

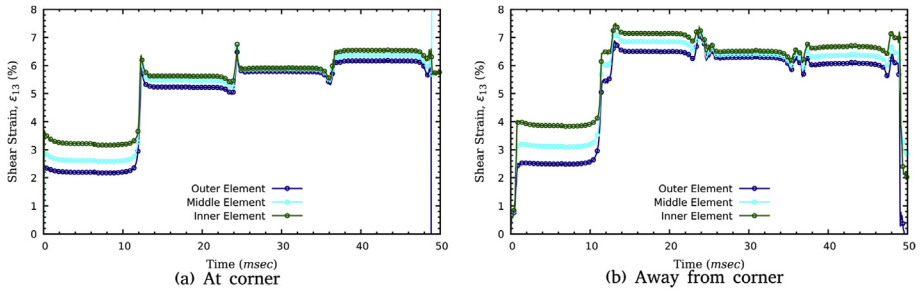

Fig. 15. Shear strain (ε_{13}) perpendicular to tool motion.

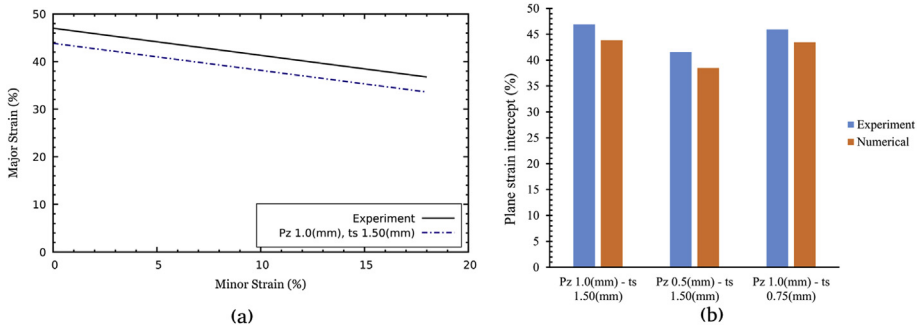

Fig. 16. Forming limit prediction by using the GTN model, (a) FLD and (b) histogram of plane strain intercept.

Table 4
Summary of parameters, strain gradient, and plane strain intercept.

Step down, Pz (mm)	Sheet thickness, ts (mm)	Strain Gradient (%)	Plane strain intercept (%)
1	1.5	7.2	44
0.5	1.5	4.6	38
1	0.75	4.8	43

results is found to be less than 10%. Therefore, the GTN model can be used for prediction of forming limits.

The hydrostatic pressure, as elaborated in section 4.2, influences formability. It is observed that for a larger step size, i.e. 1 mm as compared with 0.5 mm, higher hydrostatic pressure is obtained. This, henceforth, results in higher formability.

To the authors' knowledge, a relationship among strain gradient and formability have not been discussed in the ISF literature. Therefore, a summary of forming parameters, resultant strain gradient and predicted forming limits are shown in Table 4. A general trend is visible i.e. formability increases with an increase in strain gradient. Emmens and van den Boogaard [14] have reported that bending enhances the deformation stability and thus improves the formability. The effect of strain gradient observed herein study has a similar effect as reported by Emmens and van den Boogaard [14]. This dictates a link between strain gradient and bending. The exact relationship between these two quantities and their effect on fracture on wider range needs to be further explored.

5. Conclusions

In the present work, Finite Element models with solid elements of a straight groove test have been employed to investigate the deformation mechanics and fracture prediction capability of a GTN model. It has been shown that GTN model can be successfully applied to predict failure in incremental forming. Furthermore, deformation characteristics were found to be sensitive to the technological parameters specifically hydrostatic pressure and through thickness strain gradient.

The evolution of hydrostatic pressure and various strain components during numerical simulation of straight groove test have been investigated. The hydrostatic pressure experienced by an element directly below the tool is higher in the start and decreases with the passage of time as the tool vertically plunges into the sheet. Hydrostatic pressure is compressive in inner elements and tensile in outer elements, which suggests that fracturing in ISF if occurs, starts from the outer surface. The dimensionless damage parameter starts with an initial value of 0.0, rises in magnitude with each step down of the tool and reaches a maximum value of 1.0. The damage predicted by the GTN model is higher in outer elements as compared with inner elements. The maximum force measured at the tool increases with step down and reaches a stable zone before falling down due to fracture of the blank. Shear strain parallel to tool travel and perpendicular to tool travel is higher for elements at the inner surface as compared with elements at the outer surface. Higher values of hydrostatic pressure improve formability.

The strain gradient depends upon sheet thickness and the step-size. For the set of parameters considered in the present study, higher values of step size cause higher strain gradient which in turn improves formability. This is being reported for the first time in incremental sheet forming literature. However, a more detailed study is required for the identification of a relationship between enhanced formability and strain gradient.

Conflict of interest

The authors declare that there is no conflicts of interest.

References

[1] B.T. Araghi, G.L. Manco, M. Bambach, G. Hirt, Investigation into a new hybrid forming process: incremental sheet forming combined with stretch forming, CIRP Ann. - Manuf. Technol. 58 (2009) 225–228, https://doi.org/10.1016/j.cirp.2009.03.101.

[2] E. Hagan, J. Jeswiet, A review of conventional and modern single-point sheet metal forming methods, Proc. IME B J. Eng. Manufact. 217 (2003) 213–225, https://doi.org/10.1243/095440503321148858.

[3] J. Verbert, J.R. Duflou, B. Lauwers, Feature based approach for increasing the accuracy of the SPIF process, Key Eng. Mater. 344 (2007) 527–534, https://doi.org/10.4028/www.scientific.net/kem.344.527.

[4] Y. Li, W.J.T. Daniel, P.A. Meehan, Deformation analysis in single-point incremental forming through finite element simulation, Int. J. Adv. Manuf. Technol. 88 (2017) 255–267, https://doi.org/10.1007/s00170-016-8727-9.

[5] D.M. Neto, J.M.P. Martins, M.C. Oliveira, L.F. Menezes, J.L. Alves, Evaluation of strain and stress states in the single point incremental forming process, Int. J. Adv. Manuf. Technol. 85 (2016) 521–534, https://doi.org/10.1007/s00170-015-7954-9.

[6] T. McAnulty, J. Jeswiet, M. Doolan, Formability in single point incremental forming: a comparative analysis of the state of the art, CIRP J. Manuf. Sci.-Technol. 16 (2017) 43–54, https://doi.org/10.1016/j.cirpj.2016.07.003.

[7] S. Gatea, H. Ou, G. McCartney, Review on the influence of process parameters in incremental sheet forming, Int. J. Adv. Manuf. Technol. 87 (2016) 479–499, https://doi.org/10.1007/s00170-016-8426-6.

[8] E. Leszak, Apparatus and Process for Incremental Dieless Forming, 1967, 3342051.

[9] H. Iseki, H. Kumon, Forming limit of incremental sheet metal stretch forming using spherical rollers, J. Jpn. Soc. Technol. Plast. 35 (1994), 1336–1336.

[10] S. Matsubara, Incremental backward bulge forming of a sheet metal with a hemispherical head tool, Journal J.S.T.P. 35 (1994) 1311–1316.

[11] K. Zheng, D.J. Politis, L. Wang, J. Lin, A review on forming techniques for manufacturing lightweight complex—shaped aluminium panel components, Int. J. Lightweight Mater. Manuf. 1 (2018) 55–80, https://doi.org/10.1016/j.ijlmm.2018.03.006.

[12] Y. Kim, J. Park, Effect of process parameters on formability in incremental forming of sheet metal, J. Mater. Process. Technol. 130–131 (2002) 42–46, https://doi.org/10.1016/s0924-0136(02)00788-4.

[13] K. Jackson, J. Allwood, The mechanics of incremental sheet forming, J. Mater. Process. Technol. 209 (2009) 1158–1174, https://doi.org/10.1016/j.jmatprotec.2008.03.025.

[14] W.C. Emmens, A.H. van den Boogaard, An overview of stabilizing deformation mechanisms in incremental sheet forming, J. Mater. Process. Technol. 209 (2009) 3688–3695, https://doi.org/10.1016/j.jmatprotec.2008.10.003.

[15] K.A. Al-Ghamdi, G. Hussain, Threshold tool-radius condition maximizing the formability in SPIF considering a variety of materials: experimental and FE investigations, Int. J. Mach. Tool Manufact. 88 (2015) 82–94, https://doi.org/10.1016/j.ijmachtools.2014.09.005.

[16] L.V. Sy, Modeling of Single Point Incremental Forming Process for Metal and Polymeric Sheet, Doctoral School in Industrial Engineering, University of Padova, 2009.

[17] P.A.F. Martins, N. Bay, M. Skjoedt, M.B. Silva, Theory of single point incremental forming, CIRP Ann. - Manuf. Technol. 57 (2008) 247–252, https://doi.org/10.1016/j.cirp.2008.03.047.

[18] Y. Fang, B. Lu, J. Chen, D.K. Xu, H. Ou, Analytical and experimental investigations on deformation mechanism and fracture behavior in single point incremental forming, J. Mater. Process. Technol. 214 (2014) 1503–1515, https://doi.org/10.1016/j.jmatprotec.2014.02.019.

[19] J. Lin, Y. Liu, T.A. Dean, A review on damage mechanisms, models and calibration methods under various deformation conditions, Int. J. Damage Mech. 14 (2005) 299–319, https://doi.org/10.1177/1056789505050357.

[20] R. Zhang, Z. Shao, J. Lin, A review on modelling techniques for formability prediction of sheet metal forming, Int. J. Lightweight Mater. Manuf. 1 (2018) 115–125, https://doi.org/10.1016/j.ijlmm.2018.06.003.

[21] S. Wu, A. Reis, P. Teixeira, A.B. da Rocha, J. Lino, Damage prediction in incremental forming by using Lemaitre damage model, in: AIPConferenceProceedings1479, AIP, 2012, https://doi.org/10.1063/1.4756471.

[22] Z. Chen, X. Dong, The GTN damage model based on Hill'48 anisotropic yield criterion and its application in sheet metal forming, Comput. Mater. Sci. 44 (2009) 1013–1021, https://doi.org/10.1016/j.commatsci.2008.07.020.

[23] M. Gologanu, J.-B. Leblond, G. Perrin, J. Devaux, Recent extensions of Gurson's model for porous ductile metals, Contin. Micromech. 377 (1997) 61–130, https://doi.org/10.1007/978-3-7091-2662-2_2.

[24] M. Brunet, F. Morestin, H. Walter, Damage identification for anisotropic sheet-metals using a non-local damage model, Int. J. Damage Mech. 13 (2004) 35–57, https://doi.org/10.1177/1056789504039259.

[25] G. Hirt, J. Ames, M. Bambach, R. Kopp, R. Kopp, Forming strategies and process modelling for CNC incremental sheet forming, CIRP Ann. - Manuf. Technol. 53 (2004) 203–206, https://doi.org/10.1016/s0007-8506(07)60679-9.

[26] C.F. Guzmán, S. Yuan, L. Duchêne, E.I.S. Flores, A.M. Habraken, Damage prediction in single point incremental forming using an extended Gurson model, Int. J. Solid Struct. 151 (2018) 45–56, https://doi.org/10.1016/j.ijsolstr.2017.04.013.

[27] S. Gatea, H. Ou, B. Lu, G. McCartney, Modelling of ductile fracture in single point incremental forming using a modified GTN model, Eng. Fract. Mech. 186 (2017) 59–79, https://doi.org/10.1016/j.engfracmech.2017.09.021.

[28] J. Li, S. Li, Z. Xie, W. Wang, Numerical simulation of incremental sheet forming based on GTN damage model, Int. J. Adv. Manuf. Technol. 81 (2015) 2053–2065, https://doi.org/10.1007/s00170-015-7333-6.

[29] ASTM-E8-16a Standard Test Methods for Tension Testing of Metallic Materials, (n.d.). doi:10.1520/E0008_E0008M-16A.

[30] G. Hussain, G. Lin, N. Hayat, N.U. Dar, A. Iqbal, New methodologies for the determination of precise forming limit curve in single point incremental forming process, Adv. Mater. Res. 97–101 (2010) 126–129, https://doi.org/10.4028/www.scientific.net/AMR.97-101.126.

[31] V. Tvergaard, A. Needleman, Analysis of the cup-cone fracture in a round tensile bar, Acta Metall. 32 (1984) 157–169.

[32] V. Tvergaard, Influence of void nucleation on ductile shear fracture at a free surface, J. Mech. Phys. Solid. 30 (1982) 399–425, https://doi.org/10.1016/0022-5096(82)90025-4.

[33] J. Will, H. Nilsson, Parameter Identification of Damage Parameters of LS-DYNA GURSON Material Model from a Tensile Test, 2009.

[34] Z.-H. Zhong, Finite Element Procedures for Contact-impact Problems, Oxford University Press, 1993.

[35] J.O. Hallquist, LS-DYNA®, Theory Manual, LSTC, 2006.

[36] W.F. Hosford, R.M. Caddell, Metal Forming: Mechanics and Metallurgy, Cambridge University Press, 2011.

[37] Z. Marciniak, J.L. Duncan, S.J. Hu, Mechanics of Sheet Metal Forming, Butterworth-Heinemann, 2002.

[38] K.A. Al-Ghamdi, G. Hussain, Forming forces in incremental forming of a geometry with corner feature: investigation into the effect of forming parameters using response surface approach, Int. J. Adv. Manuf. Technol. 76 (2014) 2185–2197, https://doi.org/10.1007/s00170-014-6409-z.

[39] M. Silva, M. Skjødt, P.A. Martins, N. Bay, Revisiting the fundamentals of single point incremental forming by means of membrane analysis, Int. J. Mach. Tool Manufact. 48 (2008) 73–83.

[40] J. Smith, R. Malhotra, W.K. Liu, J. Cao, Deformation mechanics in single-point and accumulative double-sided incremental forming, Int. J. Adv. Manuf. Technol. 69 (2013) 1185–1201, https://doi.org/10.1007/s00170-013-5053-3.

[41] S.P. Keeler, W.A. Backhofen, Plastic instability and fracture in sheet stretched over rigid punches, ASM Trans. Q. 56 (1963) 25–48.